Sublithospheric small-scale convection and its implications for the residual topography at old ocean basins and the plate model

Jinshui Huang[1] and Shijie Zhong
Department of Physics, University of Colorado, Boulder, Colorado, USA

Received 25 April 2004; revised 6 January 2005; accepted 31 January 2005; published 19 May 2005.

[1] The seafloor topography and heat flux differ significantly from the predictions of the half-space cooling (HSC) model at old ocean basins. Understanding the deviations has important implications for thermal evolution of oceanic lithosphere and large-scale mantle dynamics. A widely used model that explains significant fraction of the deviations is the plate model, but the dynamical feasibility of the plate model has never been demonstrated. In this study, we investigated the effects of sublithospheric small-scale convection (SSC) and of internal heating on seafloor heat flux and topography and mantle thermal structure, and we examined the dynamic feasibility of the plate model by formulating high- resolution two-dimensional numerical models of mantle convection with strongly temperature- and depth-dependent rheology. We found that mantle convection with tectonic plates often leads to formation of a broad thermal anomaly below old lithosphere where the mantle is not cooled by subducted slabs and heat transfer is less efficient because of thick lithosphere, especially when significant internal heating is present. This trapped heat may exist in the middle mantle when the SSC is absent, and it may also be redistributed by the SSC to shallow depths to reheat the lithosphere and to homogenize mantle temperature. When internal heating accounts for $>\sim$60% of the total heat output, the trapped heat may provide sufficient heat supply to preferentially reheat old lithosphere via SSC while maintaining uniform mantle temperature. We suggest that the trapped heat and the SSC are responsible for the residual heat flux and topography at old ocean basins relative to the HSC model predictions. Our models also show that for the plate model to be dynamically viable, both the SSC and significant internal heating (>60%) are necessary. This is because only the SSC in a mantle with significant internal heating can erode and reheat the lithosphere while maintaining a nearly constant mantle temperature below lithosphere, which is the basic assumption of the plate model. With the viscosity structure and internal heating rate for the present-day mantle, we think that the plate model is dynamically viable.

Citation: Huang, J., and S. Zhong (2005), Sublithospheric small-scale convection and its implications for the residual topography at old ocean basins and the plate model, *J. Geophys. Res.*, *110*, B05404, doi:10.1029/2004JB003153.

1. Introduction

[2] Seafloor topography and heat flux are the key observations that constrain the dynamics of the mantle and lithosphere. Seafloor topography and heat flux show clear dependence on the age of seafloor, and can be explained to the first order in terms of conductive cooling and thermal contraction of oceanic lithosphere as the lithosphere ages and moves away from mid-ocean ridges [e.g., *McKenzie*, 1967; *Parsons and Sclater*, 1977; *Lister et al.*, 1990]. In particular, it has been suggested that a half-space cooling (HSC) model reproduces seafloor topography for seafloors younger than 70 Ma [*Parsons and Sclater*, 1977; *Stein and Stein*, 1992] and heat flux data for seafloor younger than 110 Ma [*Lister et al.*, 1990] (Figure 1). However, for older seafloor the observations show reduced dependence on the age in comparison with the HSC model predictions [*Parsons and Sclater*, 1977; *Stein and Stein*, 1992; *Lister et al.*, 1990] (Figure 1). For example, at the oldest part of the Pacific, the seafloor topography can be 2–3 km shallower than the HSC model prediction [e.g., *Panasyuk and Hager*, 2000]. The deviation of seafloor topography from the HSC is often referred as to residual/dynamic topography [*Davies and Pribac*, 1993; *Panasyuk and Hager*, 2000].

[3] The origin of the deviations of seafloor topography and heat flux from the HSC model at relatively old seafloor has been a subject of debate in the last three decades. Although the seafloor topography was explained in terms of models with no thermal origins [e.g., *Phipps Morgan and Smith*, 1992], there are mainly two proposals that are aimed

[1]Now at Department of Geophysics, School of Geodesy and Geomatics, Wuhan University, Wuhan, China.

0148-0227/05/2004JB003153$09.00

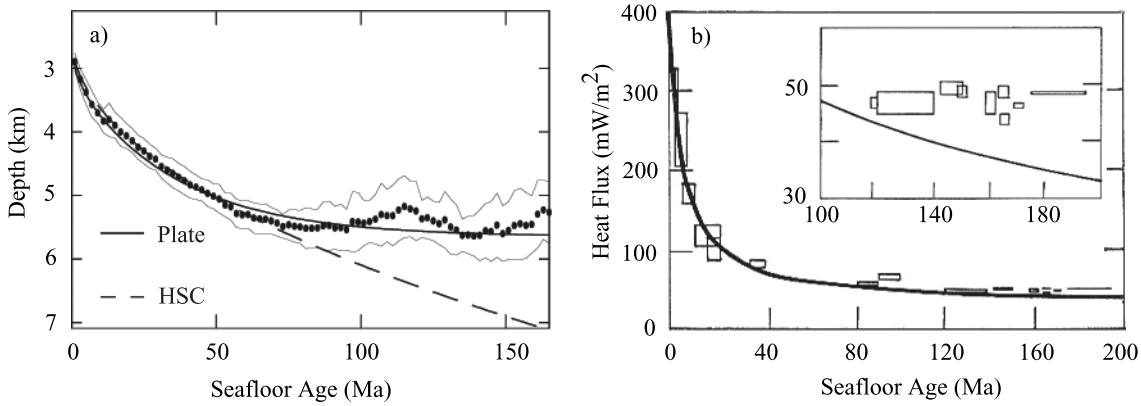

Figure 1. (a) Age-dependent seafloor topography and (b) heat flux. Figure 1a modified from *Stein and Stein* [1992] (with permission from Nature Publishing Group), and Figure 1b is modified from *Davaille and Jaupart* [1994] with data from *Lister et al.* [1990]. Also shown in Figures 1a and 1b are the HSC predictions. The topography from the plate model by *Stein and Stein* [1992] is also plotted in Figure 1a. The inset in Figure 1b is the zoom-in heat flux for seafloor older than 100 Ma.

at explaining simultaneously the seafloor topography and heat flux. First, the deviations are attributed to thermal boundary layer (TBL) instabilities that may occur dynamically below relatively old lithosphere (also called sublithospheric small-scale convection or SSC) [*Parsons and Sclater*, 1977; *Parsons and McKenzie*, 1978; *Yuen and Fleitout*, 1985; *Davaille and Jaupart*, 1994]. The SSC destabilizes the bottom part of lithosphere and replaces it with the relatively hot mantle fluid, thus preventing the lithosphere from continuous cooling as predicted by the HSC model. A closely related and also widely used model is the plate model in which it is assumed that the lithosphere overriding a mantle with a constant temperature T_m, reaches a constant thickness D_L as it ages [*Parsons and Sclater*, 1977; *Stein and Stein*, 1992]. The two parameters in the plate model, T_m and D_L, can be determined from fitting the observed seafloor topography and/or heat flux [e.g., *Turcotte and Schubert*, 2002] (Figure 1a). It is worthwhile to note that seafloor topography and heat flux anomalies can also be explained with constant heat flux plate model [*Doin and Fleitout*, 2000; *Dumoulin et al.*, 2001]. The plate model explicitly requires that basal heat flux be supplied to the lithosphere. Although the SSC is often invoked as the physical mechanism for the plate model to maintain constant T_m and D_L and to supply the basal heat flux [*Parsons and McKenzie*, 1978; *Davaille and Jaupart*, 1994], the dynamical feasibility of the plate model has never been explicitly demonstrated.

[4] Second, the deviations are believed to be caused by convective processes associated with the deep mantle, in particular the mantle upwelling plumes [*Schroeder*, 1984; *Davies*, 1988a; *Davies and Pribac*, 1993; *Malamud and Turcotte*, 1999]. Mantle plumes were initially proposed to explain the midplate volcanism [*Wilson*, 1963]. Mantle plumes result from the TBL in the deep mantle possibly at the core-mantle boundary (CMB) [*Morgan*, 1972] and the plume mode of convection is necessary for cooling the core [e.g., *Davies*, 1988a; *Sleep*, 1990]. Mantle plumes due to their buoyancy forces may produce topographic highs, and the best example is probably the Hawaiian swell topography that is suggested to result from the Pacific plate moving over the Hawaiian plume [*Davies*, 1988a; *Sleep*, 1987, 1990; *Ribe and Christensen*, 1994]. The residual topographies in the Pacific and Africa have much larger horizontal extents than the Hawaiian swell [e.g., *Panasyuk and Hager*, 2000], and they are called superswells [*Nyblade and Robinson*, 1994; *McNutt*, 1998]. These superswells are often attributed to buoyancy forces of superplumes [*Lithgow-Bertelloni and Silver*, 1998; *Romanowicz and Gung*, 2002]. Mantle plumes are also hypothesized to provide the basal heat flux for the plate model, but as many as 5000 plumes are needed [*Malamud and Turcotte*, 1999].

[5] Although the mantle plume and the SSC models are sometimes presented as competing models for the seafloor topography and heat flux anomalies, seismic observations indicate that both mantle plumes [*Wolfe et al.*, 1997; *Romanowicz and Gung*, 2002; *Montelli et al.*, 2004] and SSC [*Katzman et al.*, 1998; *Ritzwoller et al.*, 2004; *Gilbert et al.*, 2003] be important processes in the mantle. This suggests that the seafloor topography and heat flux anomalies cannot be attributed exclusively to either mantle plume or the SSC process. It is therefore important to assess the relative roles of the SSC and mantle plumes in the thermal evolution of oceanic lithosphere.

[6] The SSC/plate model that includes lithospheric age as the sole variable can account for a significant fraction of but not all the residual topography [e.g., *Panasyuk and Hager*, 2000], indicating that some of the residual topography is related to other age-independent processes (e.g., mantle plumes). In fact, the residual topography with the plate model as a reference highlights the anomalies in the southern Pacific, while greatly reducing the anomalies in the western Pacific [e.g., *Panasyuk and Hager*, 2000], which is consistent with the seismic observations of thermal plumes in the southern Pacific [*Romanowicz and Gung*, 2002; *Montelli et al.*, 2004]. Modeling the long-wavelength geoid suggests that some of the residual topography should have a deep origin, because of the depth-dependent sensitivity of the geoid [*Hager and Richards*, 1989; *Ricard and Vigny*, 1989; *Thoraval and Richards*, 1997; *Lithgow-*

Bertelloni and Richards, 1998]. However, the magnitude of the required topography to explain the geoid is uncertain [e.g., *Panasyuk and Hager*, 2000].

[7] While there is little doubt that the SSC can enhance heat flux at relatively old seafloor, questions were raised as to whether or not the SSC can actually lead to a reduced topography. *O'Connell and Hager* [1980] pointed out that by enhancing the heat flux at old seafloor, the SSC should enhance the cooling of the mantle below. Because the topography is sensitive to the integrated buoyancy in the lithosphere and mantle, *O'Connell and Hager* [1980] suggested that the SSC may not necessarily lead to a reduced topography. This argument was strengthened by *Davies* [1988b], who showed with numerical models that the SSC indeed led to larger topography than that produced from the buoyancy of the top thermal boundary layer. The cooling of the mantle from the SSC is also evident in experimental studies of SSC by *Davaille and Jaupart* [1994]. These studies present a significant challenge to the SSC/plate models in that the isothermal mantle below the lithosphere, the basic premise of the plate model, may be questionable.

[8] On the other hand, it is unclear whether or not all the residual topography and heat flux can be attributed to mantle plumes. Among all the plumes, the Hawaiian plume in the Pacific has perhaps the strongest surface manifestation with volcanic chains superimposed on a ~1000 km across and ~1.3 km high topographic swell [*Davies*, 1988a; *Sleep*, 1990]. However, the number of plumes in the mantle and their strength are not well constrained [*Courtillot et al.*, 2003; *Montelli et al.*, 2004]. For the Pacific, *Montelli et al.* [2004] identified Samoa, Tahiti, and Solomon plumes in the southern Pacific near Tonga. However, the Pacific superswell topography with a length scale of ~7000 km is largely in the western Pacific and the largest residual topography (>2.5 km [*Panasyuk and Hager*, 2000]) is in the oldest part of the Pacific. It is questionable that the entire superswell is caused by these plumes. In the Atlantic, mantle plumes seem to be preferentially located below relatively young seafloor near the mid-ocean ridge [e.g., *Jellinek et al.*, 2003]. Although thick sediments in the Atlantic complicate the topography corrections, the residual topography also shows significant deviations at old seafloor from the HSC model predictions [e.g., *Panasyuk and Hager*, 2000], suggesting that mantle plumes are not the only sources for the deviations. In addition, mantle plumes may have only limited influences on surface heat flux, as indicated by the heat flux measurements along and across the Hawaiian volcanic chain [*von Herzen et al.*, 1989] and numerical modeling of plume-plate interaction [*Ribe and Christensen*, 1994].

[9] Therefore we believe that it is important to investigate the SSC and its roles in cooling the mantle and modifying surface topography and heat flux and to examine whether or not the plate model is dynamically attainable, which are the main focus of this paper. Several new developments in the last decade motivated this study. First, recent seismic observations of mantle structures provide more evidence for the SSC. Using ScS reverberations and frequency-dependent travel times, *Katzman et al.* [1998] determined significant upper mantle structure with wavelengths of ~1000 km between the Hawaii and Tonga corridor. With the surface wave tomography, *Ritzwoller et al.* [2004] showed that the Pacific lithosphere and upper mantle with age older than ~70 Ma is on average hotter than the HSC predictions and that the general characteristics of the seismic structure is consistent with those from a mantle with the SSC. In the continental regions, the SSC with wavelengths of ~800 km is suggested for the upper mantle below the western US on the basis of topographic variations at the 410-km and 670-km discontinuities that are derived from receiver function analyses [*Gilbert et al.*, 2003]. Second, our understanding on the dynamics of the SSC has been improved significantly with new modeling techniques in both experimental and numerical studies. In particular, a significant finding is the important control of rheological activation energy on the onset of the SSC [*Davaille and Jaupart*, 1994; *Conrad and Molnar*, 1999; *Dumoulin et al.*, 2001; *Korenaga and Jordan*, 2003; *Huang et al.*, 2003; *Zaranek and Parmentier*, 2004] and temperature anomalies associated with the SSC [*Davaille and Jaupart*, 1994; *Huang et al.*, 2003; *Solomatov and Moresi*, 2000]. This may have important implications for early models of the SSC [e.g., *Davies*, 1988b] that often use too small activation energy, due to limitations in computing technologies.

[10] In this study, we investigate the dynamics of the SSC with numerical models by focusing our efforts on the following aspects. First, using more realistic activation energy in models with flow-through boundary conditions we study the effects of SSC on heat flux and topography and on cooling of the mantle. By ignoring the complicated subduction processes, this type of models enable us to focus on the SSC effects [*Huang et al.*, 2003]. Second, we investigate the effects of phase changes and other non-Boussinesq effects in the SSC models. The cold downwellings from the SSC may depress the 670-km phase change boundary (spinel to postspinel phases). The depressed phase change boundary represents a buoyancy force that may influence the surface topography [*Thoraval et al.*, 1995]. Third, we examine the effects of internal heating with convection models in a closed box. The internal heating is not considered in the HSC model and in most of the previous SSC models, because the oldest oceanic lithosphere is <200 Ma and over this period of time, internal heating may be insignificant. However, depending on mantle circulation pattern, the mantle below the oceanic lithosphere may experience rather different thermal history than the lithosphere above.

[11] We organize the paper as follows. In the next section, we will present model formulation, boundary conditions, and rheological equations. We will then show results from models to explore the effects of Rayleigh number, internal heating, boundary conditions, and phase changes. We will discuss the implications and limitations of our results before presenting the conclusions in the last section.

2. Model Description

2.1. Governing Equations and Rheology

[12] The basic physical processes of thermal convection can be described by the conservation laws of mass, momentum, and energy. With the assumption of an incompressible mantle and Boussinesq approximation, the

Table 1. Physical and Geometrical Model Parameters

Parameters[a]	Value
Thickness of the box D[b]	10^6 (2×10^6) m
Temperature drop of the layer ΔT	1350 (2500) K
Reference density ρ_0	3.3×10^3 kg m^{-3}
Thermal diffusivity κ	10^{-6} m^2 s^{-1}
Coefficient of thermal expansion α	3×10^{-5} K^{-1}
Acceleration of gravity g	9.8 m s^{-2}
Gas constant R	8.31 J mol^{-1}
Phase change parameters (for case OB5)[c]	
Equilibrium depth for the EXPC	4.1×10^5 m
Equilibrium depth for the ENPC	6.6×10^5 m
Equilibrium temperature	1350°C
Density jumps	280 kg m^{-3}
Phase transition width	2.5×10^4 m
Clapeyron slope for the EXPC	2 MPa K^{-1}
Clapeyron slope for the ENPC	−3.5 MPa K^{-1}

[a]Since the calculations are done with nondimensional parameters, these parameters are only nominal and can be treated as typical parameters used for scaling purposes.
[b]Parentheses indicate CB cases.
[c]EXPC and ENPC represent exothermic and endothermic phase changes, respectively.

nondimensional governing equations are [e.g., *McKenzie et al.*, 1974]:

$$\nabla \cdot \mathbf{u} = 0, \tag{1}$$

$$-\nabla P + \nabla \cdot \left[\eta\left(\nabla \mathbf{u} + \nabla^T \mathbf{u}\right)\right] + RaT\mathbf{e_z} = 0, \tag{2}$$

$$\frac{\partial T}{\partial t} + \mathbf{u} \cdot \nabla T = \nabla^2 T + \gamma, \tag{3}$$

where $\mathbf{u}$, P, η, T, and γ are the velocity, pressure, viscosity, temperature, and internal heating rate, respectively; $\mathbf{e_z}$ is the unit vector in vertical direction (positive upside), and Ra is a Rayleigh number which is defined as

$$Ra = \frac{\alpha \rho_0 g \Delta T D^3}{\kappa \eta_0}, \tag{4}$$

where α is the coefficient of thermal expansion, ρ_0 is the reference mantle density, η_0 is the reference viscosity that is taken as the viscosity at the bottom boundary unless otherwise indicated, D is the thickness of the box, κ is the thermal diffusivity, $\Delta T = T_b' - T_s'$ is the temperature difference across the box with T_b' and T_s' as the bottom and surface temperature, respectively (T_s' = 273 K), and g is the gravitational acceleration. Equations (1)–(3) are obtained by using the following characteristic scales: length $[L] = D$; time $[t] = D^2/\kappa$; viscosity $[\eta] = \eta_0$; temperature $[T] = \Delta T$.

[13] We assume a Newtonian rheology for the mantle with the Arrhenius rheology law. The viscosity in dimensionless form is

$$\eta = \eta_r \exp\left(\frac{E}{T + T_{\text{off}}} - \frac{E}{1 + T_{\text{off}}}\right), \tag{5}$$

where $\eta_r = \eta_b/\eta_0$, $\eta_r = 1$ for most cases as η_b is the viscosity at the bottom boundary, $T_{\text{off}} = T_s'/\Delta T$, E is a nondimensional activation energy and is related to activation energy E' as $E = E'/(R\Delta T)$ with R as the gas constant (Table 1). We impose a cutoff of 10^6 for viscosity in our models.

2.2. Two Types of Models: OB and CB

[14] To better understand the different physical processes in our problem, it is important to formulate models that isolate different parts of physics. To accomplish this, we use two different types of two-dimensional convection models to investigate the SSC and its effects on topography and heat flux: (1) models with flow-through boundary conditions (OB) and (2) models within a closed box (CB) (Figure 2). The OB models use flow-through boundary conditions but exclude subduction processes and large-scale return flow (Figure 2a). This simplification enables us to focus on the processes of cooling of initially hot mantle, thickening of thermal boundary layer, and the subsequent development of the SSC. The OB models also allow us to compare our results easily with the HSC models, because of their close resemblance to the HSC models. However, with the flow-through boundary conditions, mantle materials do not stay in the model domain for sufficiently long time to allow us to examine the effects of internal heating in the OB models. The CB models produce more realistic flow patterns (e.g., subduction) (Figure 2b), and we will use them to examine the effects of internal heating, in addition to the SSC.

[15] The OB and CB models differ in boundary conditions (Figure 2). For the OB models, $\partial T/\partial x = 0$ is used for the outflow boundary, while $T = T_0(z, t_0) + \delta T$ is for the inflow boundary, where $T_0(z, t_0)$ is the nondimensional temperature at depth z predicted from the HSC model with nondimensional mantle interior temperature of 1 (i.e., $T_m' = T_b' = T_s' + \Delta T$ in dimensional parameters) [e.g., *Turcotte and Schubert*, 2002] for lithospheric age t_0 (10 Ma is used in this study), and δT is the small random perturbation (5×10^{-3}). The top boundary is prescribed with a nondimensional plate velocity V_p, while the bottom boundary is fixed. The horizontal velocity at the inflow and outflow boundaries $V_b(z)$ is the velocity of a Couette flow for a variable viscosity fluid [*Turcotte and Schubert*, 2002]. Although a Couette flow assumes no horizontal pressure gradient, horizontal pressure gradient may arise in the interior of flow, because a Couette flow is only applied at the inflow and outflow boundaries.

[16] For the CB models, reflecting boundary conditions are used on the sidewalls. While the surface is prescribed with a plate velocity, the bottom boundary is free slip. Furthermore, we introduced a weak zone at each corner near the surface in which the viscosity is reduced by about 4 orders of magnitude, relative to the lithosphere (Figure 2b). For both OB and CB models, temperatures at the top and bottom boundaries are 0 and 1, respectively. To eliminate the effects of initial conditions, all the model calculations for the OB and CB models are done until a statistically steady state is reached.

[17] It is worthwhile to point out that similar two-dimensional (2-D) models to our CB models with prescribed surface velocity and weak zones have been formulated previously elsewhere with different emphases [e.g., *Davies*, 1989; *Zhong and Gurnis*, 1994; *King et al.*,

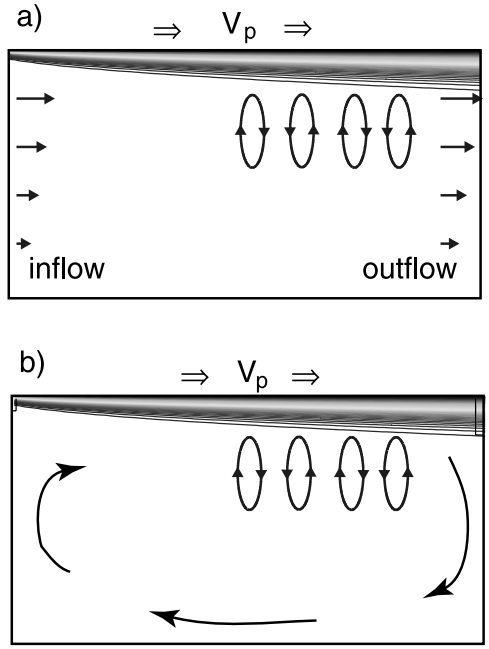

Figure 2. Schematic diagrams of the two types of 2-D models employed in this study: (a) flow-through boundary (OB) model and (b) closed box (CB) model.

1992; *Bunge et al.*, 1998; *Dumoulin et al.*, 2001]. Our approach here with a prescribed plate motion simplifies the calculations of lithospheric age and comparison with the HSC models, but the plate motion is not as dynamic as in some of the previous studies [e.g., *King et al.*, 1992; *King and Hager*, 1990; *Zhong and Gurnis*, 1995; *Conrad and Hager*, 1999] in which a variety of proxies for plate margin processes are used to model plate motion. However, understanding the physical processes that are important to plate margin dynamics remains a great challenge in geodynamics [*Bercovici*, 2003]. In this study, while using a prescribed plate motion, we also vary other parameters (e.g., mantle viscosity) to examine the robustness of our results.

[18] The governing equations are solved with a finite element code Citcom [*Moresi and Solomatov*, 1995; *Moresi and Gurnis*, 1996] with some extensions [*Zhong et al.*, 2000]. For most of our calculations, we use a box with aspect ratio of 14 and 768 × 96 finite elements for the OB models and aspect ratio 6 with 384 × 96 finite elements for the CB models unless specified otherwise. A larger aspect ratio is used for the OB models than that for the CB models, because the OB models are designed to simulate the plate-induced shear flow with no return flow. The elements are refined near the boundary layers to better resolve the development of the TBL instabilities.

[19] In addition to these models with the Boussinesq approximation, we have also computed a set of models with non-Boussinesq effects including phase changes (olivine to spinel and spinel to postspinel) and their associated latent heat, adiabatic and frictional heating. The governing equations for these models are the same as those of *Christensen and Yuen* [1985], and numerical implementations are given by *Zhong and Gurnis* [1994].

2.3. Topography and Heat Flux From the Numerical and HSC Models

[20] An important feature of this study is the direct comparison of the surface topography and heat flux between numerical and the HSC models. For the HSC model, surface heat flux and topography are controlled by the differential temperature between the mantle and the surface, $T'_m - T'_s$ [*Turcotte and Schubert*, 2002]. Suppose that the nondimensional interior temperature is $T_m = (T'_m - T'_s)/\Delta T$, the nondimensional topography w_{HSC} normalized by $D\alpha\Delta T$, as a function of horizontal position from the spreading center, x, and plate velocity, V_p, is

$$w_{\mathrm{HSC}} = 2T_m\left(\frac{x}{\pi V_p}\right)^{1/2}, \tag{6}$$

where we did not consider the water in the calculations. The nondimensional heat flux Q_{HSC} is

$$Q_{\mathrm{HSC}} = T_m\left(\frac{V_p}{\pi x}\right)^{1/2}, \tag{7}$$

where Q_{HSC} is normalized by $k\Delta T/D$, and k is the thermal conductivity.

[21] For the OB models, $T_m = 1$, as $T'_m = T'_b$. However, for the CB models, because of the bottom thermal boundary layer, T'_m is often not equal to T'_b, and T_m is determined by averaging the mantle temperature excluding the top and bottom TBLs and subduction zone as we will explain later. Therefore (6) and (7) can be used to determine the HSC model predictions for surface topography and heat flux for the OB and CB models for a given T_m.

[22] Determinations of actual surface topography and heat flux from the numerical models, either the OB or CB models, are straightforward. For example, the nondimensional surface topography that is scaled in the same way as that in the HSC models is related to nondimensional normal stress acting on the surface σ_{zz} and Ra as $w = \sigma_{zz}/Ra$ (notice that σ_{zz} varies with x). Another useful measure from convection models is the isostatic topography w_{iso} [*Jarvis and Peltier*, 1982; *Davaille and Jaupart*, 1994] which is defined in this study as

$$w_{\mathrm{iso}} = \int_{1-d_{\mathrm{iso}}}^{1} [T(x,z) - T_m]dz, \tag{8}$$

where d_{iso} is a compensation depth. For a HSC model, w_{iso} is the same as that in (6) if d_{iso} is set to be sufficient large; w_{iso} may differ from w from convection models, because the topographic response to thermal structure is depth- and viscosity-dependent and not completely isostatic [e.g., *Parsons and Daly*, 1983; *Hager and Richards*, 1989].

[23] *Jarvis and Peltier* [1982] and *Davies* [1988b] were probably the first to compare the topography and heat flux from convection models to those from the HSC (or boundary layer) models. *Jarvis and Peltier* [1982] formulated steady state isoviscous convection models in a unit aspect ratio box, while *Davies*' [1988b] models use either uniform viscosity or weakly temperature-dependent viscosity (a

Table 2. Parameters and Statistics of the Models

Case	$Ra \times 10^7$	$Ra_i \times 10^7$	γ	E', J mol^{-1}	θ	L	Q_t[a]	Q_b	T_m	x_{onset}[b]	$x_{\text{p-onset}}$
OB1	5	4.39	0	120	7.60	14	12.4	0.58	0.984	4.1	3.7
OB2	5	4.35	0	90	5.76	14	12.7	0.86	0.978	3.4	2.9
OB3	5	4.52	0	180	11.25	14	12.1	0.29	0.992	5.7	5.1
OB4[c]	5	3.32	0	120	8.03	14	12.4	0.34	0.952	3.9	4.9
OB5[d]	5	4.48	0	120	7.60	14	12.4	0.27	0.986	4.0	3.7
CB1	100	2.53	0	120	13.66	6	17.3	17.1	0.541	-	20.2
CB2	200	10.6	0	120	11.48	6	19.6	19.0	0.600	-	7.1
CB3	400	24.5	0	120	11.07	6	21.3	21.9	0.613	3.6	4.0
CB4	50	10.9	10	120	7.84	6	22.3	12.1	0.749	4.7	6.0
CB5	100	27.6	10	120	7.31	6	25.4	15.2	0.780	3.7	3.1
CB6	200	62.3	10	120	7.03	6	27.0	16.9	0.797	1.9	1.8
CB7	25	19.1	20	120	5.20	6	30.4	9.6	0.945	4.6	3.5
CB8	50	33.5	20	120	5.44	6	30.8	11.0	0.921	3.1	2.4
CB9	100	65.3	20	120	5.50	6	31.8	12.2	0.916	1.8	1.6
CB10	200	122	20	120	5.63	6	32.2	13.8	0.904	1.2	1.0
CB11	200	89.1	20	120	6.27	4	35.0	16.4	0.851	1.5	1.3

[a] Q_t and Q_b are the averaged heat flux at the surface and bottom boundaries. T_m is the averaged upper mantle temperature.
[b] The parameters x_{onset} and $x_{\text{p-onset}}$ are the SSC onset positions measured from the models and predicted from the scaling law by *Huang et al.* [2003], respectively. In using the scaling for the CB cases that use a larger box thickness, we converted parameters to be consistent with those by *Huang et al.* [2003].
[c] This case uses a layered viscosity structure.
[d] This case uses two phase changes.

factor of 10 viscosity variation) and a larger aspect ratio box. However, their HSC (or boundary layer) model heat flux and topography are determined by fitting the surface heat flux and topography in the middle portion of the box to $t^{1/2}$ dependence like (6) and (7). We construct our HSC model by using averaged mantle temperature T_m from numerical models. As we will see later, convection models may produce entirely different dependence of heat flux/topography on x or age from that of the HSC models. Sometimes, fitting to the HSC or boundary layer model may not be always feasible.

3. Results

3.1. SSC From OB Models

[24] First we study the effects of the SSC on heat flux and topography by computing a set of OB models with E varying from 8.02 to 16.04 (i.e., from 90 to 180 kJ mol^{-1}), Ra varying from 5×10^6 to 5×10^8 and V_p varying from 1584 to 3169 (i.e., 5 to 10 cm yr^{-1}). Other parameters are included in Table 1. In these calculations, we set η_r in equation (5) to be 1. Compared to those obtained in laboratory studies [*Karato and Wu*, 1993], our models used relatively small activation energy, and this is because we use a Newtonian rheology to approximate a non-Newtonian rheology [*Christensen*, 1984].

[25] We now present a selected set of the OB models (Table 2). We first present a representative case that has E = 10.70 (or 120 kJ mol^{-1}), $Ra = 5 \times 10^7$ and $V_p = 2535$ (or 8 cm yr^{-1}) (case OB1 in Table 2). A snapshot of a steady state temperature structure shows that the thermal boundary layer thickens with the distance from the in-flow boundary and that the SSC starts at $x \sim 4$ (Figures 3a and 3b), consistent with the onset scaling $\tau_c = 62.6 Ra_i^{-0.68}\theta^{0.74}$ of *Huang et al.* [2003], where Ra_i is the Rayleigh number defined by the interior viscosity and $\theta = E/(T_m + T_{\text{off}})^2$ is the Frank-Kamenetskii parameter (Table 2). This pattern of thermal structure is representative and does not change significantly in time. The SSC produces significant vertical flow with a maximum vertical velocity of 2947 (or 9.3 cm yr^{-1}) at a depth of 0.3, comparable to V_p and horizontal flow velocity at this depth.

[26] Surface heat flux decreases with the distance from the inflow boundary (or age), but surface topography determined from the surface normal stress increases with age, as expected (Figures 3c and 3d). The SSC produces small undulations in both surface heat flux and topography. We also compute the topography and heat flux from the HSC model by using equations (6) and (7) with the prescribed V_p and $T_m = 1$. The heat flux agrees well with that from the HSC model except at large ages where the SSC elevates the heat flux (Figure 3d). Importantly, in spite of the SSC and its cooling of the mantle, the topography is nearly identical to that from the HSC model (Figure 3c).

[27] The deviations of heat flux from the HSC model are larger for smaller activation energy E (Figures 4a and 4b for E = 8.02, 10.70, and 16.04 or 90, 120, and 180 kJ mol^{-1}. Cases OB1-3 in Table 2). This is because with a smaller E, the SSC can erode a larger portion of the lithosphere, thus leading to a larger surface heat flux. Although the heat flux after the onset of SSC is always larger than that from the HSC model, the surface topography does not differ significantly from the HSC model (Figures 4c and 4d).

[28] To understand better the relation between the SSC and topography, we further analyzed temperature structure. In comparison with the HSC model, the SSC results in a higher temperature in the bottom portion of lithosphere but a smaller temperature in the mantle interior (Figure 3b for horizontally averaged temperature-depth profiles at different horizontal locations or ages). That is, the SSC causes heat exchange between the mantle and lithosphere. We also computed the isostatic topography on the basis of thermal structure with different compensation depths d_{iso}. For d_{iso} = 1/8 for the representative case, the isostatic topography includes only the buoyancy in the lithosphere and shallow upper mantle and shows much smaller topography at old ages after the onset of SSC than that from the HSC model (Figure 3c). When d_{iso} is increased to include a larger

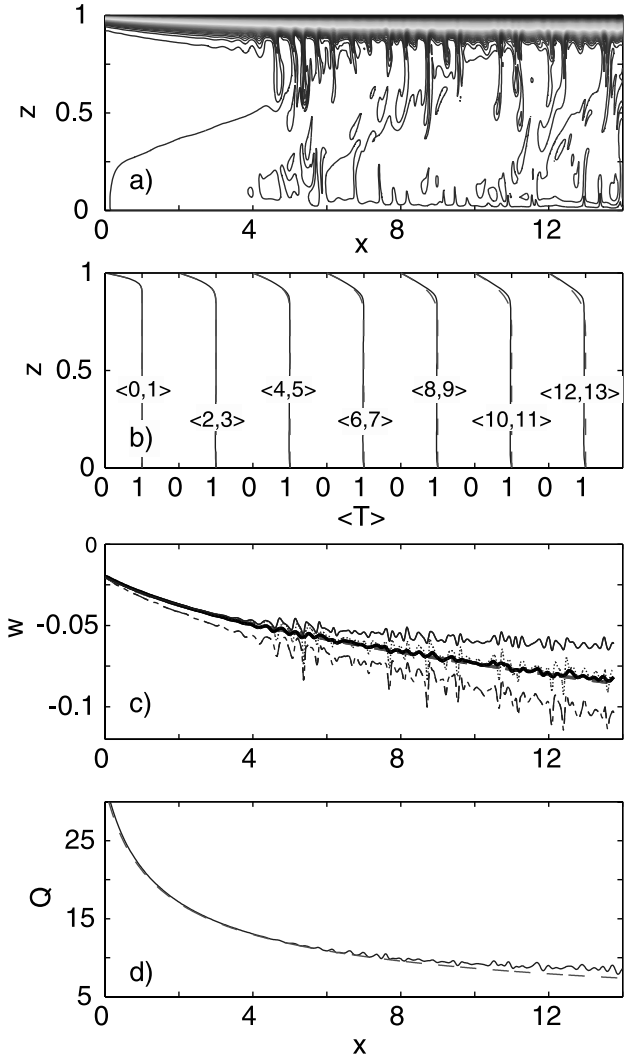

Figure 3. (a) A snapshot of temperature field, (b) the horizontally averaged temperature $\langle T \rangle$ at different horizontal locations versus the depth, (c) surface topography and isostatic topography, and (d) surface heat flux for case OB1. In Figure 3b, the numbers in the angle brackets for each line indicate the horizontal section over which the averaged temperature is computed. The dashed lines in Figures 3b and 3d are predictions from the HSC model. In Figure 3c, the thick solid and dashed lines (almost overlapped each other) are the topography from the numerical model and the HSC model, respectively, and the thin solid, dotted, and dashed lines represent the isostatic topography with d_{iso} = 1/8, 1/2, and 1, respectively.

portion of convective mantle, the isostatic topography increases relative to that with $d_{\rm iso}$ = 1/8. For $d_{\rm iso}$ = 1/2, the isostatic topography is nearly identical to that of the HSC model, and for a larger $d_{\rm iso}$, the isostatic topography is even larger than that of the HSC model. This is consistent with the SSC's effects of cooling on the mantle and of heating on the lithosphere. *Davaille and Jaupart* [1994] showed that the isostatic topography is reduced significantly after the onset of the SSC. However, their isostatic topography included only buoyancy contributions from the top thermal boundary layer (i.e., lithosphere) not the mantle which may be important for the topography as we just showed.

[29] *Solomatov and Moresi* [2000] suggested that the SSC should have comparable vertical and horizontal flow velocity. Because in our models the horizontal flow is influenced not only by the SSC but also the imposed plate motion, it is important to examine how the vertical and horizontal velocities compare to each other. We found that the vertical velocity of the SSC is similar in magnitude to V_p and horizontal flow velocity of the SSC. For cases OB1-3 and other similar cases (not shown), the ratios of maximum horizontal to vertical velocities at a depth of 0.3 where the SSC is significant may range from 1.28 to 1.97. However, for all these cases, the modeled topography and heat flux show similar age dependence to that in Figure 4.

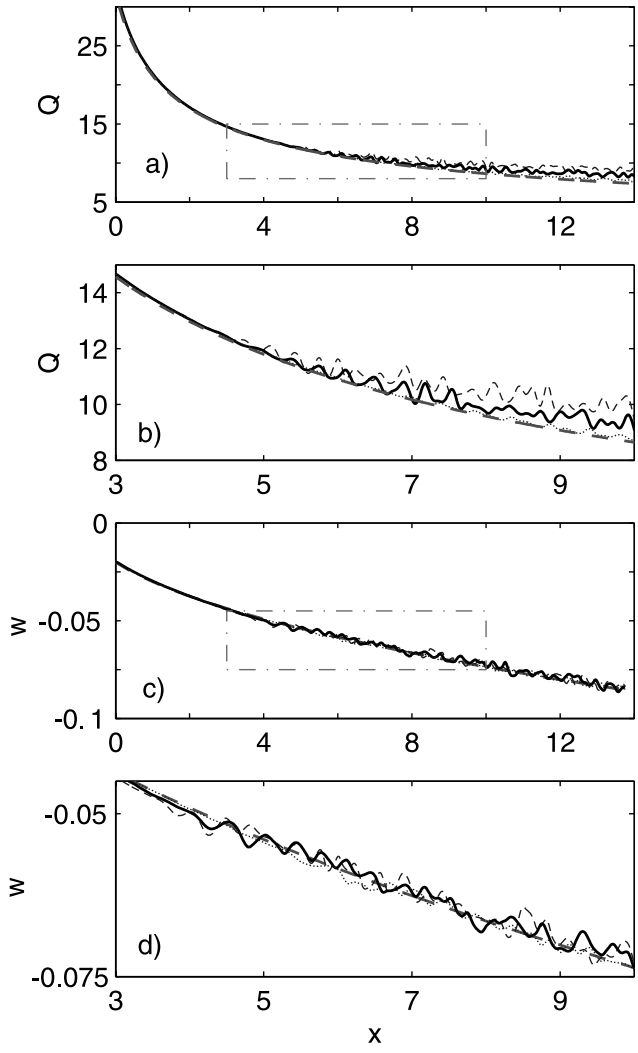

Figure 4. (a, b) Surface heat flux and (c, d) topography from cases OB1-3 with different activation energy. Figures 4b and 4d are the zoom-ins of Figures 4a and 4c. The thick dashed lines are from the HSC model, while the thick solid, thin solid, and thin dotted lines are for E = 120, 90, and 180 kJ mol^{-1}, respectively.

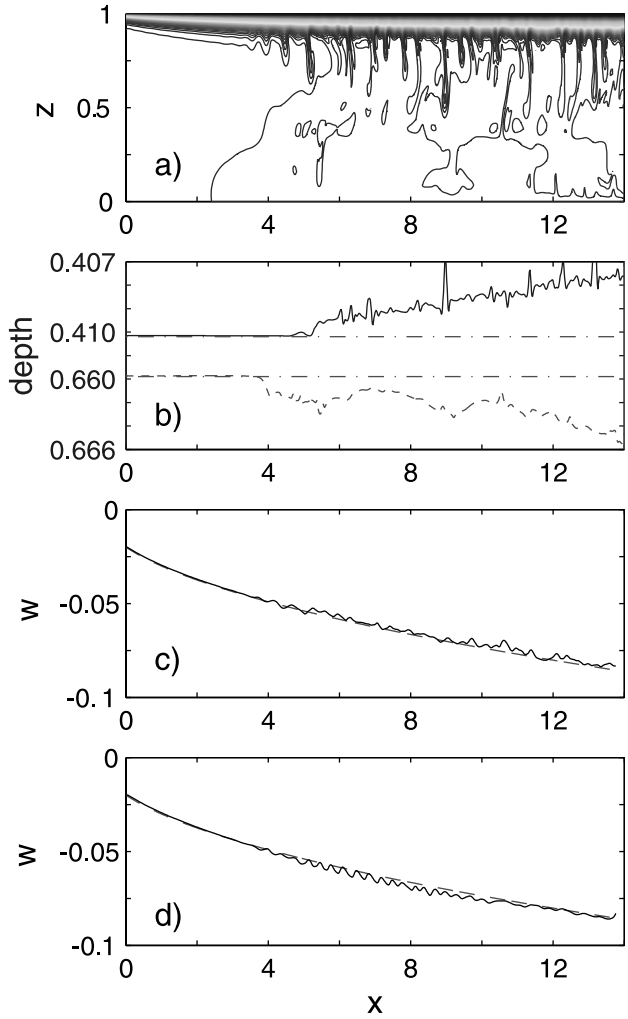

Figure 5. (a) A snapshot of temperature field, (b) phase boundary deflections, (c) surface topography for case OB4 with the effects of phase changes, latent heat and viscous heating included, and (d) the topography for case OB5 with a stratified viscosity structure. The dashed lines in Figures 5c and 5d are from the HSC model.

3.2. Non-Boussinesq and Stratified Viscosity Effects in OB Models

[30] The mantle structure with its stratified viscosity [*Hager and Richards*, 1989] and solid-solid phase changes is more complicated than what was assumed in models presented in the last section. Phase changes may affect mantle dynamics in two different ways [*Christensen and Yuen*, 1985]. (1) Lateral temperature anomalies cause the phase boundary to deflect from its equilibrium position, and this leads to buoyancy force that may affect mantle flow. (2) The latent heat associated with the phase changes may affect mantle temperature. In this section, we examine the effects of phase changes and stratified viscosity on surface topography in the SSC models. Because the effects of frictional heating are on the same order as the latent heat [*Christensen and Yuen*, 1985], our models include both latent heat and frictional heating effects.

[31] For models with phase change effects, we included both the 410-km and 660-km phase changes (Table 1 for the phase change parameters). We repeated cases OB1-3 in last section but with phase changes. No significant difference was observed between the models with and without phase changes. Figures 5a–5c show the temperature structure, deflections at the 410-km and 660-km phase boundaries, and surface topography for case OB4 with $E = 10.70$ (i.e., 120 kJ mol^{-1}) (Table 2). As expected, the cooling of the mantle by the SSC elevates the 410-km phase boundary while depressing the 660-km phase boundary. However, there is no significant topography difference from the HSC model (Figure 5c).

[32] We then examine the effects of stratified viscosity by computing a case (case OB5 in Table 2) that includes a stratified viscosity with $\eta_r = 1$, 10, and 100 for the upper mantle, transition zone, and lower mantle, respectively. This viscosity structure is generally consistent with that inferred from the studies of the geoid [e.g., *Hager and Richards*, 1989]. $Ra = 5 \times 10^7$ for Ra that is defined by the reference viscosity in the upper mantle. For this case, the phase changes are not considered, given their relatively small roles (Figures 5a–5c). Again, we observe no significant effects of the SSC on the topography, relative to that from the HSC model (Figure 5d).

[33] In summary of the results from OB models, the SSC may enhance heat transfer and produce elevated heat flux at old lithosphere, but the SSC's effects on surface topography are minimal. Compared with the HSC model, the SSC increases the temperature near the base of lithosphere but cools the underlying mantle. These results are rather insensitive to non-Boussinesq effects and stratified viscosity structure.

3.3. CB Models With No Internal Heating

[34] Although our OB models effectively simulate the physical processes of the top TBL including its instabilities, with no return flow and subduction the flow patterns in these models are simplified (Figure 2a). We now consider the second type of models, the more realistic CB models that include return flow, subduction, and internal heating (Figure 2b). For models in this section, we use a two-layer viscosity structure that has a viscosity increase of a factor of 60 at the 660-km depth (Table 1 for other parameters), but the phase changes and frictional heating are ignored. The activation energy E is equal to 120 kJ mol^{-1}.

[35] We first present three models with no internal heating (i.e., $\gamma = 0$) and $V_p = 5070$ (i.e., 8 cm/year) but different Ra (cases CB1-3 in Table 2 with $Ra = 10^9$, 2×10^9 and 4×10^9). Notice that in defining Ra, we use the upper mantle viscosity at temperature $T = 1$ as a reference viscosity, and that the physically more meaningful Rayleigh number Ra_i defined by the average upper mantle viscosity (excluding the subduction zone) can be much smaller because $T < 1$ in the upper mantle (Table 2). When the surface velocity is prescribed as a boundary condition, it is often desired to examine the dynamic compatibility between the prescribed surface velocity and interior viscosity and thermal structures [e.g., *Zhong and Gurnis*, 1994]. One may study the compatibility by varying the prescribed surface velocity, while keeping interior viscosity structures fixed. Alternatively, one can also vary the interior structures while fixing the

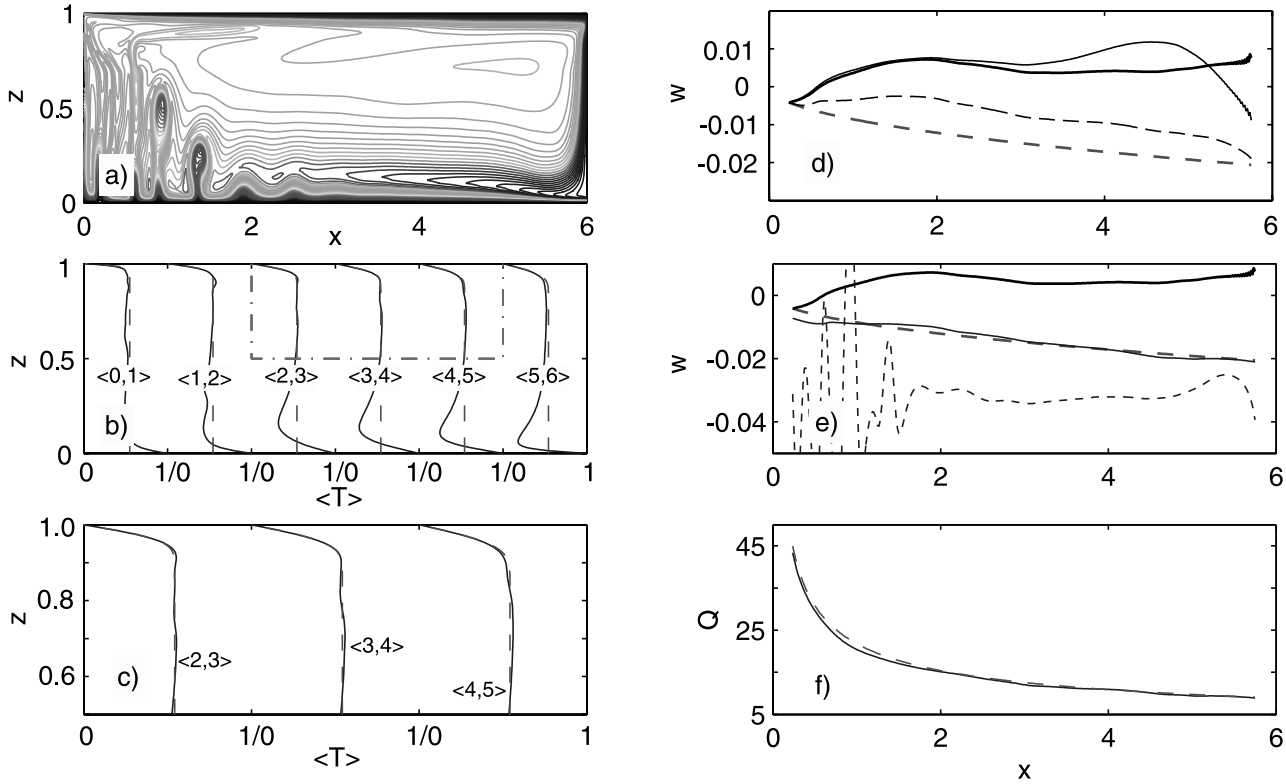

Figure 6. (a) A snapshot of temperature field, (b, c) the horizontally averaged temperature $\langle T \rangle$ at different horizontal locations versus the depth, (d) surface topography, (e) isostatic topography, and (f) surface heat flux for case CB1. In Figures 6b and 6c, the numbers in the angle brackets for each line indicate the horizontal section over which the averaged temperature is computed. Figure 6c is for a zoom-in region in Figure 6b. The dashed lines in Figures 6b, 6c, and 6f are from the HSC model. In Figure 6d, the thick solid and dashed lines are the topography from the numerical and HSC models, respectively, while thin solid line is from a calculation with temperature in the bottom 1/4 of the box that is set to be 1, and thin dashed line is from a calculation with free-slip top boundary. In Figure 6e, the thick solid and dashed lines are the topography from the numerical and HSC models, respectively, while the thin solid and dashed lines represent the isostatic topography with d_{iso} = 1/8 and 3/4, respectively.

surface velocity. We choose the latter approach by varying *Ra* or interior viscosity. However, we wish to point out that the surface velocity in fully dynamic models is influenced not only by the interior structures but also by the relatively poorly constrained plate boundary properties [*Gurnis*, 1989; *King and Hager*, 1990; *Davies*, 1989]. Therefore it is often difficult to determine precisely which pair of parameters of *Ra* and surface plate velocity is more appropriate.

[36] For case CB1 with $Ra = 10^9$, we observe that upwelling plumes or sheets form and rise from the bottom TBL, while no TBL instability (or SSC) develops from the top boundary layer (Figure 6a). The averaged surface and bottom heat flux are 17.3 and 17.1, respectively (Table 2). Since this case does not have any internal heating, these two heat fluxes should be identical. The slight difference may reflect small temporal fluctuation or/and slight under-resolution at the bottom boundary layer. According to the scaling law for the onset of SSC by *Huang et al.* [2003], Ra_i and E (which determines the Frank-Kamenetskii parameter θ) for this case suggest that the SSC does not develop, given the length of the box (Table 2). We observe a broad thermal anomaly in the midmantle below the old lithosphere (Figures 6a, 6b, and 6c). We think that this thermal anomaly may arise for two reasons: (1) this region is not cooled by subducted slab because of its large distance from the subduction zone, and (2) the old and thick lithosphere makes heat transfer less efficient. This thermal anomaly was not observed in any of our OB models, because with the flow-through boundary conditions mantle flow stays in the model domain only for a fixed period of time. We may refer this hot thermal anomaly in the CB models to as trapped heat. The trapped heat has significant effects on surface topography and causes the topography at old lithosphere to be higher than that at the young lithosphere (Figure 6d). This unrealistic topography pattern can also be seen from the isostatic topographies for different $d_{\rm iso}$ (Figure 6e). When $d_{\rm iso}$ is sufficiently large, the isostatic topography is higher at old lithosphere than that at young lithosphere.

[37] Thermal structure at large depths has relatively small effects on surface topography, because its buoyancy is largely compensated onto the bottom boundary [e.g., *Hager and Richards*, 1989]. This is evident from the similarity in topographies that result from the thermal structure in the whole box and from the thermal structure of the top 3/4 of box (i.e., the topography is computed with the temperature

in the bottom 1/4 of the box that is set to 1) (Figure 6d). The prescribed plate motion may produce horizontal pressure difference that affects surface topography [*Turcotte and Schubert*, 2002; *Phipps Morgan and Smith*, 1992]. This effect can be estimated by comparing the topographies from models with prescribed plate motion and free-slip top boundary. This effect is inversely dependent on asthenospheric viscosity. For case CB1 with relatively small *Ra* (i.e., large asthenospheric viscosity), this effect is moderate (Figure 6d), but it is rather small for all the other cases that we considered in this study.

[38] Like in the OB models, it is important to define a corresponding HSC model with which we can compare our results. As shown in equations (6) and (7), in order to use the HSC model, we need to define an average mantle temperature T_m. However, for the CB models it is not always clear how to define a HSC model, because the mantle temperature is not constant (e.g., Figures 6a and 6b). We compute the average temperature in a region from z = 0.5 to the bottom of the top TBL in vertical direction and excluding the subduction zone in the horizontal direction. We use this average temperature as T_m to compute the HSC predictions. For this case, T_m is found to be 0.541 (Table 2). The HSC model prediction for temperature and surface topography are shown as dashed lines in Figures 6b and 6d, respectively. While the temperature from the HSC agrees well with the numerical model in the top thermal boundary layer, their difference is clear in the fluid interiors, particularly for the broad hot anomaly (i.e., trapped heat) in the midmantle below the old lithosphere (Figure 6c for enlarged version of Figure 6b). Surface heat flux is generally consistent with the HSC model, except for the young lithosphere at $x \sim 1$ where the actual heat flux is slightly less (Figure 6f). This is caused by the smaller temperature below the young lithosphere.

[39] When *Ra* is doubled to 2×10^9 (i.e., the reference viscosity is reduced by a factor of two while other parameters are fixed), the average surface and bottom heat flux are increased to 19.6 and 19.0, respectively (case CB2 in Table 2), and the averaged temperature T_m is 0.600. Again for this case, no SSC is expected to develop in the box, according to the scaling law of *Huang et al.* [2003] (Table 2). This is supported by the thermal structure that shows no SSC (Figure 7a). Compared to case CB1, the increased *Ra* leads to a larger heat flux, and with no SSC, the increase in heat flux is largely accomplished by the increase in mantle temperature T_m. The broad hot anomaly or trapped heat is also reduced significantly (Figures 7a and 7b). This has significantly effects on the topography that now shows the normal trend of subsidence with lithospheric age, although the topography remains significantly smaller than the HSC model prediction (Figure 7c), due to the trapped heat (Figures 7a and 7b). Again, the surface heat flux is consistent with the HSC model (Figure 7d), similar to case CB1.

[40] When *Ra* is doubled again to 4×10^9, the average surface and bottom heat flux are increased to 21.3 and 21.9, respectively (case CB3 in Table 2), and T_m is 0.613. We now observe the SSC that starts on average at $x \sim 3.6$ (Figure 7e), which is comparable with the predicted $x = 4.0$ for onset from the scaling law (Table 2). Compared to case CB2, T_m does not change much, and the increased heat flux is largely caused by the SSC below old lithosphere (x > 3.6) and strong plume activities that bring significant heat to the shallow mantle below young lithosphere (Figures 7e and 7f). This is supported by the surface heat flux that is uniformly higher than the HSC model prediction (Figure 7h). Notice that the SSC causes clear deviations in temperature from the HSC model near the base of lithosphere (Figure 7f), similar to the SSC in the OB models. Importantly, the topography subsides more rapidly with x or age than the HSC prediction (Figure 7g), opposite to the preceding cases with smaller *Ra*. The isostatic topography for $d_{iso} = 3/4$ shows similar trend (Figure 7g). We think that this is caused by the combining effects of the SSC and strong plume activities. The SSC helps release the trapped heat below old lithosphere and increases (i.e., deepens) the topography at old lithosphere, while strong plume activities bring heat to the young lithosphere (Figure 7e) that lifts the topography at the young lithosphere. For this case, the pressure effect caused by the plate motion is minor (Figure 7g).

[41] The CB models with no internal heating demonstrate that surface topography may deviate significantly from the HSC model prediction with or without the SSC. However, when the SSC is absent at relatively small *Ra*, heat may be accumulated below old lithosphere to form broad and long-wavelength thermal anomalies and this trapped heat may cause much smaller topography at old lithosphere than predicted from the HSC model.

3.4. CB Models With Internal Heating

[42] We have computed total seven cases with internal heating rate varying from 10 to 20 and *Ra* varying from 2.5×10^8 to 2×10^9, while other parameters are kept the same as those used in cases CB1-3 in section 3.3. Case CB4 has a homogeneous internal heating rate $\gamma = 10$ and $Ra = 5 \times 10^8$ (Table 2). The average heat flux at the surface and bottom is 22.3 and 12.1, respectively, indicating that internal heating accounts for 45% of the total surface heat flux. Ideally, the differential heat flux between the surface and bottom boundaries should be equal to the internal heating rate γ. However, there is a small difference (i.e., 10.2 versus 10) for this case, indicating some but not severe numerical errors. T_m is 0.749. The SSC is predicted to start at $x \sim 6.0$, the same as the box length (Table 2). However, we observe intermittent SSC that happens very close to the right side boundary or the subduction zone (Figure 8a). The overall thermal structure including the upwellings and the broad thermal anomalies below old lithosphere (i.e., the trapped heat) (Figures 8a and 8b) is similar to that in case CB1 with no internal heating (Figure 6a). It is therefore not surprising to see the more elevated topography at old lithosphere than that at young lithosphere (Figure 8c). Similar to case CB1, surface heat flux agrees well with the HSC model, except for the young lithosphere where the actual heat flux is slightly less (Figure 8d) due to the smaller temperature in the underlying mantle (Figure 8a).

[43] When *Ra* is doubled to 10^9 but γ remains to be 10, the averaged surface and bottom heat flux are 25.4 and 15.2, respectively (i.e., 40% internal heating) (case CB5 in Table 2), and T_m is 0.780. The SSC begins at $x \sim 3.7$, which is slightly larger than the predicted $x \sim 3.1$ from the scaling for the onset (Figure 8e and Table 2). Compared

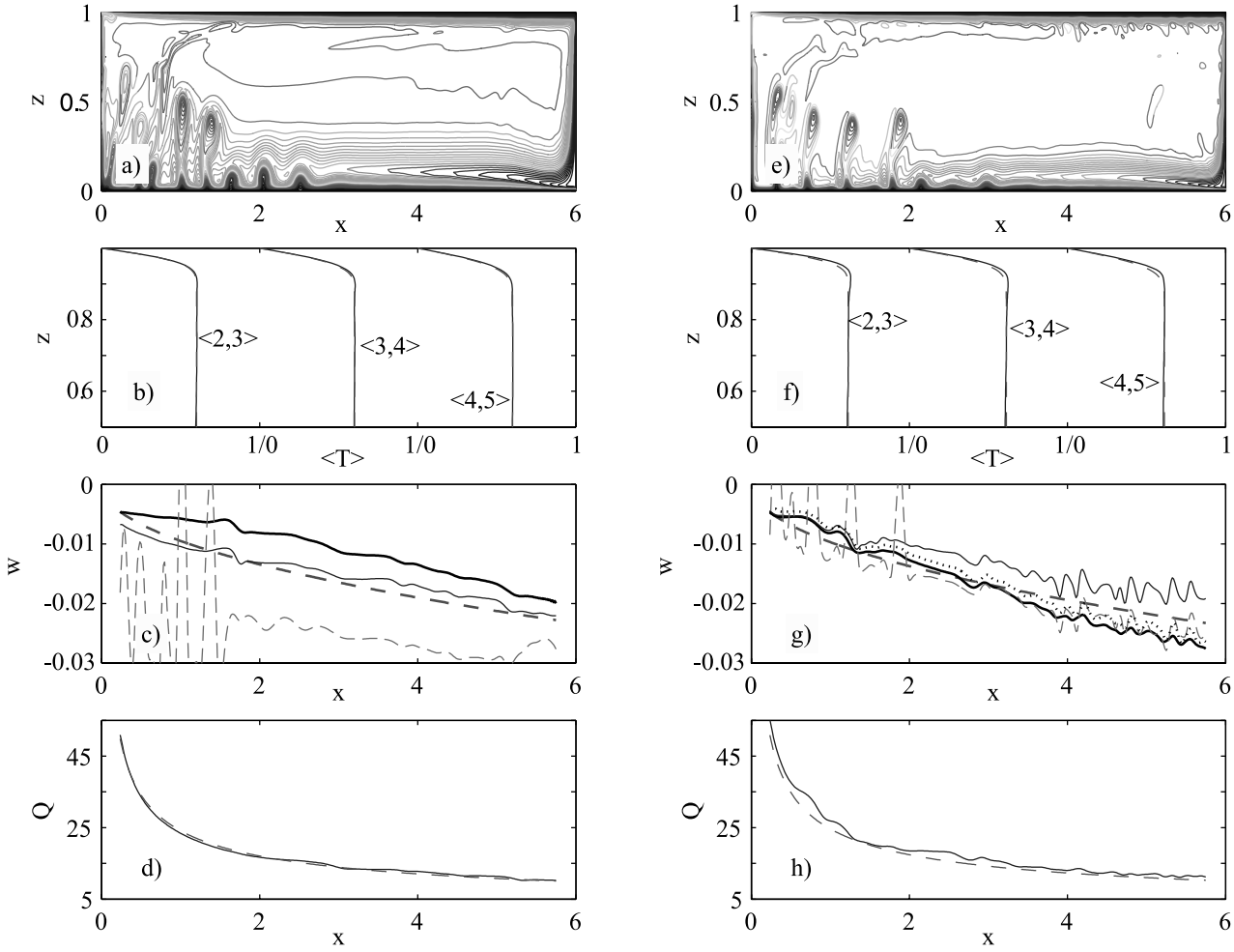

Figure 7. (a) A snapshot of temperature field, (b) the horizontally averaged temperature $\langle T \rangle$ at different horizontal locations versus the depth, (c) surface topography and isostatic topography, and (d) surface heat flux for case CB2, and (e–h) the corresponding plots for case CB3. The line conventions are the same as those in Figure 6 except that in Figure 7g the dotted line is for a calculation with free-slip top boundary.

with case CB4 with $Ra = 5 \times 10^8$, the increased Ra leads to ~14% increase in surface heat flux (Table 2), significant portion of which is attributed to the SSC. The SSC cools the mantle and homogenizes the mantle temperature (Figures 8e and 8f). The broad hot anomaly that exists in case CB4 with no significant SSC now largely disappears, although some still exists before the SSC develops (Figures 8e and 8f). After the SSC develops, the temperature near the bottom of lithosphere is much higher than that from the HSC model, while the interior temperature remains the same as the HSC model (Figure 8f). The topography is uniformly smaller than that from the HSC model (Figure 8g), largely because of the trapped heat, as indicated by the thermal structure (Figures 8e and 8f) and isostatic topography (Figure 8g). Surface heat flux agrees well with the HSC model prediction (Figure 8h).

[44] When Ra is further increased to 2×10^9 with $\gamma = 10$, the averaged surface and bottom heat flux are increased to 27.0 and 16.9, respectively (i.e., 37% internal heating) (case CB6 in Table 2), and T_m is 0.797. With the increased Ra, the SSC begins at $x \sim 1.9$ (Table 2). The SSC leads to more homogeneous mantle temperature (Figures 9a and 9b). The topography is nearly identical to the HSC model prediction (Figure 9c). Compared to the HSC model, while the isostatic topography with $d_{iso} = 1/8$ shows reduced topography at large x or age as a result of the SSC, the isostatic topography with $d_{iso} = 3/4$ indicates a steeper subsidence with x (Figure 9c). In combining with depth-dependent topography response [*Parsons and Daly*, 1983; *Hager and Richards*, 1989], this thermal structure causes surface topography to be nearly identical to the HSC model prediction for this case. However, this perfect agreement is more of a coincidence because of the particular choice of model parameters used for this case. Surface heat flux is noticeably larger at the old lithosphere than the HSC model because of the effects of SSC (Figure 9d).

[45] We also computed a set of calculations with $\gamma = 20$ and Ra varying from 2.5×10^8, 5×10^8, 10^9, and 2×10^9 (cases CB7-10) but all the other parameters are identical to the preceding internal heating cases. Cases with $\gamma = 20$ generally have ~60% internal heating, which is probably more realistic for the Earth given that our internal heating includes both radiogenic heating and the heating from secular cooling [e.g., *Davies and Richards*, 1992]. The

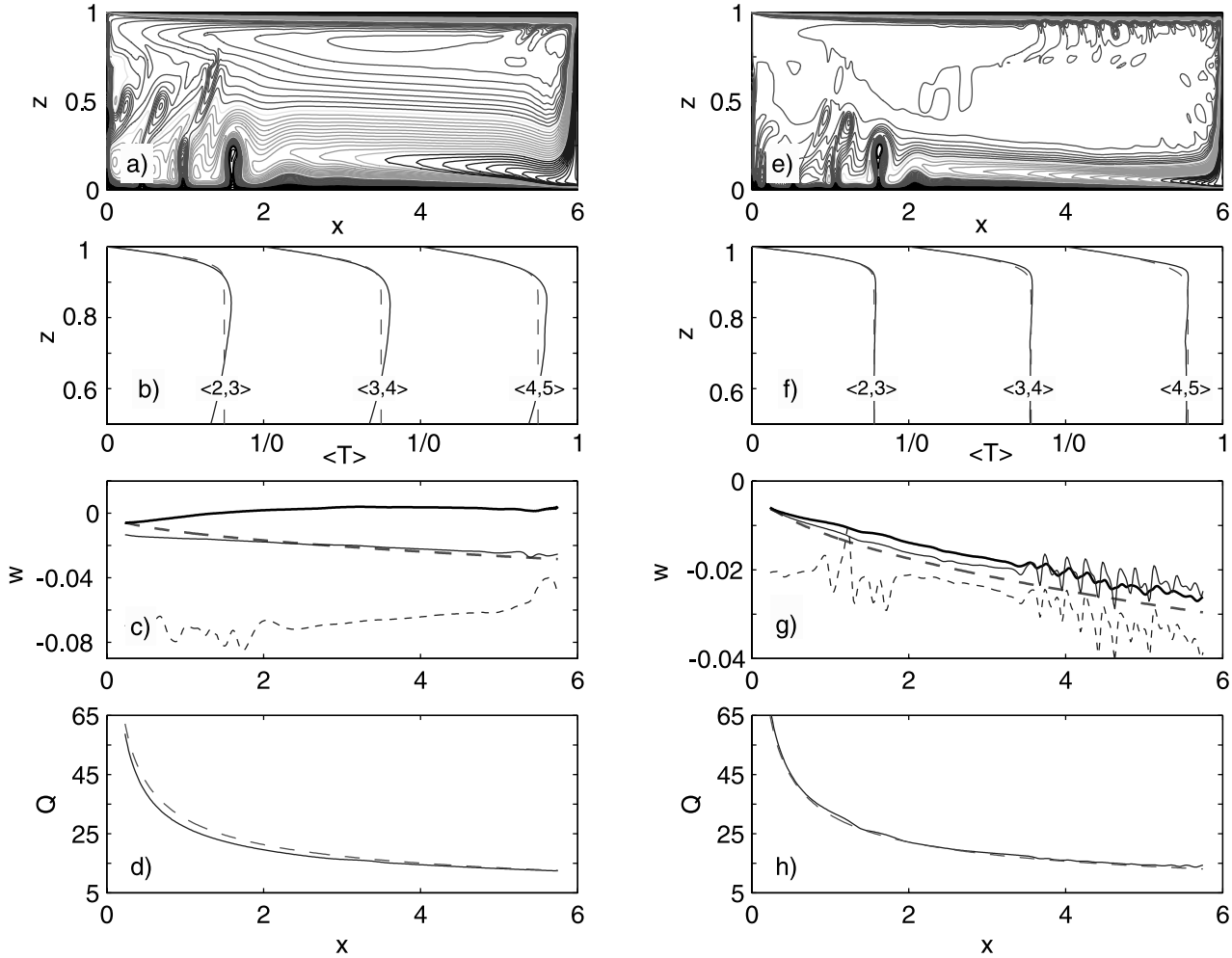

Figure 8. (a) A snapshot of temperature field, (b) the horizontally averaged temperature $\langle T \rangle$ at different horizontal locations versus the depth, (c) surface topography and isostatic topography, and (d) surface heat flux for case CB4, and (e–h) the corresponding plots for case CB5. The line conventions are the same as those in Figure 6.

general results for the trapped heat in the mantle below old lithosphere and the SSC are similar to those from cases CB4-6 with smaller internal heating. However, these cases with larger internal heating rate produce surface heat flux and topography that are more consistent with the plate model.

[46] For case CB7 with $Ra = 2.5 \times 10^8$ (Table 2), T_m is 0.945 and the SSC begins at $x \sim 4.6$ (Table 2). Because of the relatively late onset of the SSC, the trapped heat produces significantly reduced topography relative to the HSC model prediction, similar to the preceding cases with smaller γ (e.g., case CB5 in Figure 8g). When Ra increases, the SSC becomes more intense and starts at earlier times (Table 2). The SSC releases the trapped heat below relatively old lithosphere and homogenizes the mantle temperature, while eroding the bottom portion of lithosphere and reheating the lithosphere.

[47] For $Ra = 2 \times 10^9$ and $\gamma = 20$ (case CB10 in Table 2), T_m is 0.904, and the SSC begins at $x \sim 1.2$, which is similar to the predicted $x \sim 1.0$ from the scaling for the onset (Figure 10a and Table 2). While the mantle temperature is largely uniform, the SSC significantly increases the temperature near the base of lithosphere (Figures 10a and 10b) and surface heat flux (Figure 10e), relatively to the HSC model. Surface topography is significantly reduced after the onset of SSC, compared with the HSC model, although the topography does not "flatten" completely (Figure 10c). This is consistent with the isostatic topography (Figure 10c). Again, the plate motion-induced pressure effect on surface topography is relatively small (Figure 10d). We observed similar results for case CB9 with $Ra = 10^9$ and $\gamma = 20$ (Table 2), in which the SSC begins at $x \sim 1.8$.

[48] Different from the preceding cases with $\gamma = 0$ or 10 (cases CB1-6) in which the intense SSC at large Ra often leads to surface topography at old lithosphere that is either identical to or larger (i.e., deeper) than that from the corresponding HSC model predictions (Figures 7g and 9c for cases CB3 and CB6, respectively), for $\gamma = 20$ the intense SSC always leads to reduced topography at old lithosphere (e.g., Figure 10c for case CB10). This result is insensitive to box size. We computed case CB11 which is identical to case CB10 except for the aspect ratio which is reduced to 4 (Table 2). For this case, the SSC starts at $x \sim 1.5$ (Figure 10f), which is slightly larger than that for case

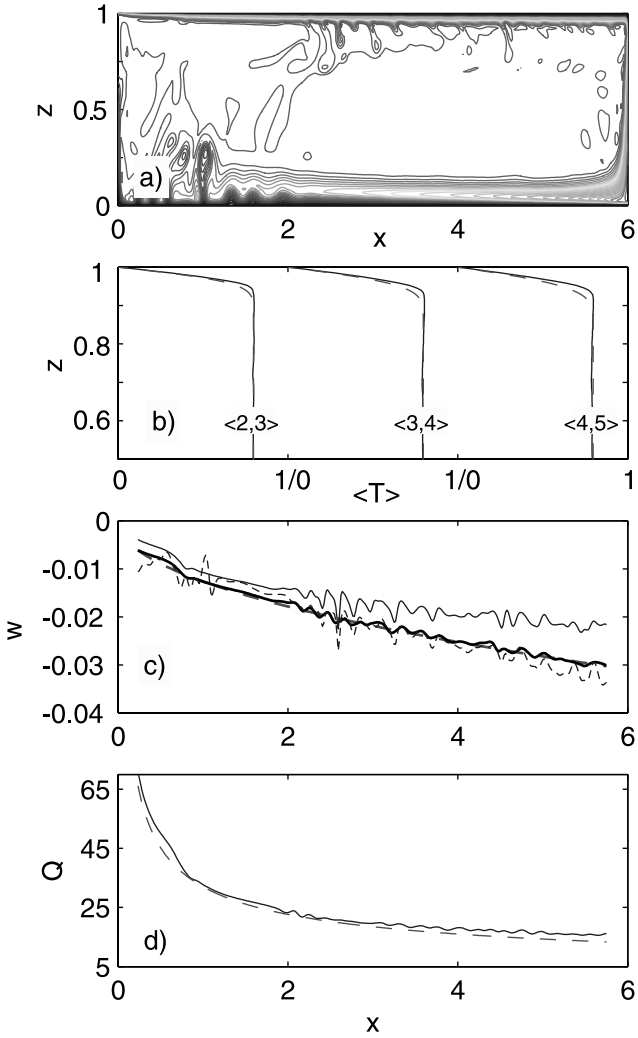

Figure 9. (a) A snapshot of temperature field, (b) the horizontally averaged temperature $\langle T \rangle$ at different horizontal locations versus the depth, (c) surface topography and isostatic topography, and (d) surface heat flux for case CB6. The line conventions are the same as those in Figure 6.

CB10, mainly because of the change in interior temperature and viscosity as a result of reducing the aspect ratio (Table 2). The smaller aspect ratio also leads to a larger averaged heat flux, as the averaged lithospheric age is smaller (Table 2). We observe similarly reduced surface topography and elevated heat flux at relatively old lithosphere because of the SSC (Figures 10g and 10h).

4. Discussions

[49] The main objective of this study is to understand the origin of the reduced topography and enhanced heat flux at old seafloor relative to the HSC model, in particular the roles of the SSC in thermal evolution of oceanic lithosphere and the dynamic viability of the plate model. Using the OB models with flow-through boundary conditions, we demonstrated that the SSC alone does not lead to reduced topography at old seafloor, although it can increase the heat flux (Figures 3 and 4). The SSC erodes the bottom portion of lithosphere and mixes it with the underlying mantle. This process heats up the lithosphere but cools the underlying mantle. As a result, surface heat flux is increased. However, surface topography may not change that much because the topography is controlled by the integrated buoyancy structure of the entire mantle that may not be modified significantly by the SSC. These results from OB models are in general consistent with what *O'Connell and Hager* [1980] and *Davies* [1988b] had suggested for the potential effects of the SSC on cooling the mantle and deepening surface topography. These results also show that the SSC may not necessarily lead to the plate model, because the cooling of the mantle by the SSC-eroded material may not give rise to a uniform mantle temperature below lithosphere that is required by the plate model. In order for the plate model to be dynamically viable, additional mechanism that can heat the SSC-eroded material to the background uniform mantle temperature is necessary. Such a mechanism should supply preferentially more heat to the mantle below the relatively old lithosphere where the SSC may take place. Our CB models in a closed box provide important clues on how this mechanism may operate dynamically self-consistently.

[50] Our CB models show that heat may be accumulated below relatively old lithosphere where the mantle is not cooled by subducted slabs and heat transfer is less efficient because of thick lithosphere (e.g., Figures 6a and 8a). The trapped heat can be produced in models with or without internal heating and is commonly observed in 2-D and 3-D convection models with tectonic plates [e.g., *Lowman and Gable*, 1999; *King et al.*, 2002; *Lowman et al.*, 2003]. The trapped heat forms a broad thermal anomaly in the mantle below the old lithosphere when the SSC is absent (e.g., Figures 6a and 8a for cases CB1 and CB4). When the SSC is present at relatively large *Ra*, the trapped heat may provide a heat reservoir to reheat the old lithosphere via the SSC while maintaining relatively uniform mantle temperature (e.g., Figures 8e, 10a, and 10e). The trapped heat can significantly reduce the surface topography (i.e., to lead to shallower topography) relative to the HSC model at very long wavelengths (e.g., Figures 6d, 7c, 8c, and 8g).

[51] The SSC tends to enhance the heat transfer and to release the trapped heat by mixing it with the relatively cold fluids eroded from the old lithosphere. This process also reheats the lithosphere and homogenizes mantle temperature. For models with small internal heating ratio (<40%), the intense SSC plus strong plume activities below young lithosphere may cause surface topography to be identical to or even deeper than that from the HSC model (Figures 7g and 9c for cases CB3 and CB6). However, when internal heating rate is increased to ~60% (Figures 10c and 10g for cases CB9-11), even with the intense SSC, surface topography remains significantly reduced at old lithosphere, relatively to the HSC models, consistent with the observations [*Lister et al.*, 1990; *Stein and Stein*, 1992]. The topography and heat flux from these models are also consistent with the plate model with constant basal heat flux of *Dumoulin et al.* [2001]. In these models, the interaction between the trapped heat and the SSC preferentially reheats the old lithosphere while maintaining a relatively uniform mantle temperature (Figures 10b and 10f). Therefore we suggest that in order for the plate model to be

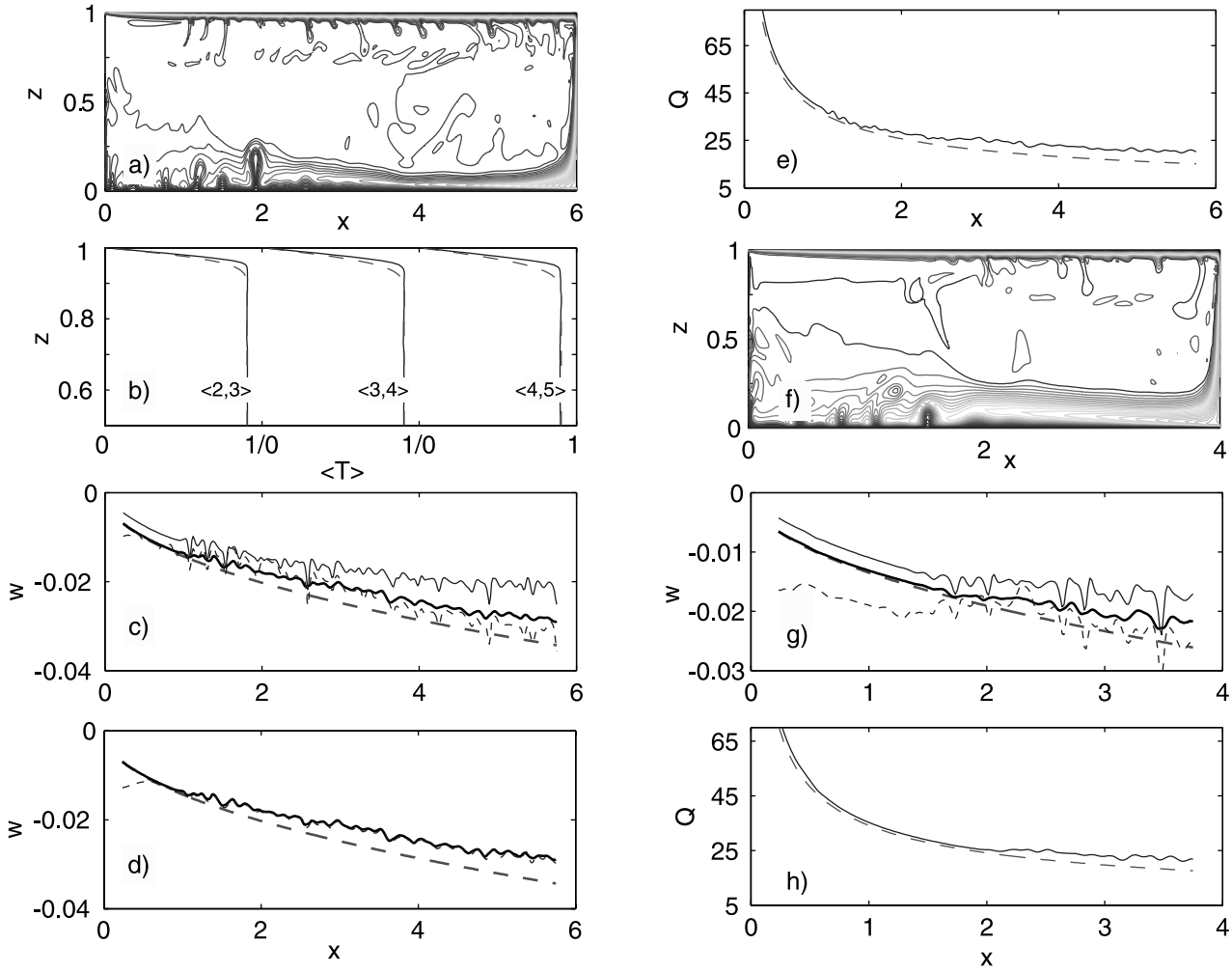

Figure 10. (a) A snapshot of temperature field, (b) the horizontally averaged temperature $\langle T \rangle$ at different horizontal locations versus the depth, (c) surface topography and isostatic topography, (d) surface topography for a calculation with free-slip top boundary (thin dashed line), and (e) surface heat flux for case CB10, and (f–h) the corresponding plots for case CB11. The line conventions are the same as those in Figure 6.

dynamically viable, both intense SSC and significant internal heating are necessary. Internal heating in our models includes both radiogenic heating and the heating from secular cooling. Although debatable, we think that 60% internal heating ratio required for the plate model may be reasonable for the mantle [*Davies and Richards*, 1992].

[52] The trapped heat over a large region below old lithosphere, whether it is in the middle mantle when the SSC is absent or it is vertically redistributed by the SSC, produces elevated topographic anomalies at very long wavelengths, relative to the HSC model. We suggest that the trapped heat contributes significantly to the broad and long-wavelength residual topography (i.e., the superswell topography), particularly in the western Pacific [e.g., *Panasyuk and Hager*, 2000] where no significant thermal plumes are detected [*Romanowicz and Gung*, 2002; *Montelli et al.*, 2004]. This proposal is also consistent with that of *Davies* [1999], who speculated the existence of broad thermal anomalies in the mantle. It is often assumed that seafloor topography should follow the prediction of the HSC model unless mantle plumes are present. Our results on the elevated topography from the trapped heat suggest that this assumption is untenable.

[53] Although the SSC/plate model provides a reasonable explanation for ocean floor residual topography and heat flux, the existence of the SSC has been a subject of debate. Using relatively realistic temperature-dependent viscosity, recent mantle convection studies, first by *Davaille and Jaupart* [1994] and then followed with important revision by *Korenaga and Jordan* [2003] and *Huang et al.* [2003], determined the rheological conditions for the upper mantle viscosity and activation energy that are needed to initiate the SSC. These studies suggest that the SSC is very likely important for the oceanic upper mantle. However, *Davies* [1988b] suggested that the SSC was insignificant because according to his convection models the SSC should lead to >1 km topographic variations at wavelengths of 600–1600 km that are not observed on Earth. However, we believe that the large topography of *Davies* [1988b] may be caused by the small activation energy in his models that leads to too large temperature anomalies for the SSC. The most important evidence for the SSC comes from different

seismic observations that reveal oceanic upper mantle structures of characteristics of the SSC [*Katzman et al.*, 1998; *Montagner*, 2002; *Ritzwoller et al.*, 2004]. High-resolution global and regional seismic models also reveal many small-scale structures that are not associated with subduction or plumes [e.g., *Kennett and Yoshizawa*, 2002; *Gilbert et al.*, 2003].

[54] Finally, it is worthwhile to point out a number of potential criticisms on this study.

[55] 1. Our 2-D models with plate motion produce transverse rolls for the SSC, while in three dimensions, the SSC should form longitudinal rolls [*Richter and Parsons*, 1975]. From 3-D models of SSC with plate motion, *van Hunen et al.* [2003] concluded that the main limitation of 2-D transverse roll models is the possibly delayed onset time for the SSC. In this study, we observe a generally good agreement on the SSC onset times with the scaling law by *Huang et al.* [2003] which was derived from 2-D longitudinal roll models with no plate motion but was found generally consistent with 3-D models by *van Hunen et al.* [2003] (Table 2). Therefore we believe that the main conclusions in this study are not sensitive to our choice of the 2-D geometry.

[56] 2. The cases with significant internal heating (>40%) lead to T_m = 0.75 or above. With the nominal ΔT = 2500 K used for these cases, the dimensional internal temperature may seem to be much higher than the observed 1350°C. However, we think that our main conclusions are robust for two reasons. First, for a given internal heating rate Cartesian models tend to give higher interior temperature than that from more realistic spherical shell models [e.g., *Zhong et al.*, 2000]. Second is due to the rescaling. Our models have three controlling nondimensional parameters *Ra*, *E,* and T_{off}. We can always change ΔT and reference viscosity in proportion to keep *Ra* the same. Our numerical experiments show that while the changes in *E* and T_{off} resulting from varying ΔT may slightly affect the onset times of SSC, our main conclusions are insensitive to the choice of ΔT.

[57] 3. We consider only steady state solutions and treat the heating from secular cooling in the same way as radiogenic heating, like what is often done in geodynamic modeling. While this approximation helps us to circumvent the initial condition problems, it is interesting for future studies to examine the validity of this approximation.

[58] 4. The trapped heat below old lithosphere is produced from our 2-D models that include only one subduction zone fixed at the sidewall of the box. However, subduction process on the Earth is more complicated with mobile trenches and subducted slabs that can go below either overriding or subducting plate. Future studies are needed to assess the effects of these complications, although *King et al.* [2002] demonstrated that the trapped heat remains significant in 3-D models with multiple plates and subduction zones that are free to go below overriding and subducting plates.

5. Conclusions

[59] In this study, we investigated the thermal evolution of oceanic lithosphere and its implications for the origin of the reduced topography and elevated heat flux at old seafloor by formulating numerical models of mantle convection with realistic temperature- and depth-dependent rheology. In particular, we examined the dynamic feasibility of the plate model by studying the effects of sublithospheric small-scale convection (SSC) and internal heating on surface heat flux and topography and mantle thermal structure. Our main findings are summarized as follows.

[60] 1. Mantle convection with tectonic plates often leads to formation of a broad thermal anomaly below old lithosphere where the mantle is not cooled by subducted slabs and heat transfer is less efficient because of thick lithosphere, especially when significant internal heating is present. This trapped heat may exist in the middle mantle when the SSC is absent, or it may be redistributed by the SSC to shallow depths to reheat the lithosphere and be partially released. We suggest that the trapped heat contribute significantly to the residual topography on seafloor, particularly in the western Pacific.

[61] 2. The SSC, by eroding the bottom part of oceanic lithosphere, reheats the lithosphere and increases surface heat flux. The SSC mixes the eroded, relatively cold fluids with the underlying mantle with trapped heat, thus homogenizing mantle temperature. When significant internal heating (>60%) is present, the trapped heat may provide sufficient heat supply to preferentially reheat old lithosphere via SSC while maintaining uniform mantle temperature. Therefore the SSC and significant internal heating explain well the elevated heat flux and reduced topography at old lithosphere relative to the HSC model predictions. For small internal heating (<40%), intense SSC may release all the trapped heat and even draw additional heat from the mantle below old lithosphere, leading to larger or more deepened topography than the HSC model prediction, especially when significant plume activities are present to bring heat to young lithosphere.

[62] 3. For the plate model to be dynamically viable, both the SSC and significant internal heating (>60%) are necessary. Only the SSC in a mantle with significant internal heating can erode the lithosphere while maintaining a constant mantle temperature below lithosphere, both of which are essential for the plate model. With the viscosity structure and internal heating rate for the present-day mantle, the plate model is dynamically viable.

[63] **Acknowledgments.** We thank P. Molnar, M. Ritzwoller, and N. Shapiro for many stimulating discussions; C. Stein for providing Figure 1a; and one of the two anonymous reviewers and Associate Editor S. Solomatov for their careful reviews. This research is supported by the David and Lucile Packard Foundation and U.S. NSF under grant EAR-0134939. J. Huang acknowledges partial support from SRF for ROCS, SEM, the Key Laboratory of Geospace Environment and Geodesy, the Ministry of Education, China (grant 1469990324233-04-09), and the Laboratory of Dynamic Geodesy, Chinese Academy of Sciences (grant L04-01).

References

Bercovici, D. (2003), Generation of plate tectonics from mantle convection, *Earth Planet. Sci. Lett.*, *205*, 107–121.

Bunge, H. P., M. A. Richards, C. Lithgow-Bertelloni, and J. R. Baumgardner (1998), Time scales and heterogeneous structure in geodynamic Earth models, *Science*, *280*, 91–95.

Christensen, U. R. (1984), Convection with pressure- and temperature-dependent non-Newtonian rheology, *Geophys. J. R. Astron. Soc.*, *77*, 343–384.

Christensen, U. R., and D. A. Yuen (1985), Layered convection induced by phase transition, *J. Geophys. Res.*, *90*, 10,291–10,300.
Conrad, C. P., and B. H. Hager (1999), Effects of plate bending and fault strength at subduction zones on plate dynamics, *J. Geophys. Res.*, *104*, 17,551–17,571.
Conrad, C. P., and P. Molnar (1999), Convective instability of a boundary layer with temperature- and strain-rate-dependent viscosity in terms of "available buoyancy", *Geophys. J. Int.*, *139*, 51–68.
Courtillot, V., A. Davaille, J. Besse, and J. Stock (2003), Three distinct types of hotspots in the Earth's mantle, *Earth Planet. Sci. Lett.*, *205*, 295–308.
Davaille, A., and C. Jaupart (1994), Onset of thermal convection in fluids with temperature-dependent viscosity: Application to the oceanic mantle, *J. Geophys. Res.*, *99*, 19,853–19,866.
Davies, G. F. (1988a), Ocean bathymetry and mantle convection: 1. Large-scale flow and hotspots, *J. Geophys. Res.*, *93*, 10,467–10,480.
Davies, G. F. (1988b), Ocean bathymetry and mantle convection: 2. Small-scale flow, *J. Geophys. Res.*, *93*, 10,481–10,488.
Davies, G. F. (1989), Mantle convection model with a dynamic plate: Topography, heat flow and gravity anomalies, *Geophys. J. Int.*, *98*, 461–464.
Davies, G. F. (1999), *Dynamic Earth: Plates, Plumes and Mantle Convection*, Cambridge Univ. Press, New York.
Davies, G. F., and F. Pribac (1993), Mesozoic seafloor subsidence and the Darwin rise, past and present, in *The Mesozoic Pacific: Geology, Tectonics, and Volcanism*, *Geophys. Monogr. Ser.*, vol. 77, edited by M. Pringle et al., pp. 39–52, AGU, Washington, D. C.
Davies, G. F., and M. A. Richards (1992), Mantle convection, *J. Geol.*, *100*, 151–206.
Doin, M. P., and L. Fleitout (2000), Flattening of the oceanic topography and geoid: Thermal versus dynamic origin, *Geophys. J. Int.*, *143*, 582–594.
Dumoulin, C., M. P. Doin, and L. Fleitout (2001), Numerical simulations of the cooling of an oceanic lithosphere above a convective mantle, *Phys. Earth Planet. Inter.*, *125*, 45–64.
Gilbert, H. J., A. F. Sheehan, K. G. Dueker, and P. Molnar (2003), Receiver functions in the western United States, with implications for upper mantle structure and dynamics, *J. Geophys. Res.*, *108*(B5), 2229, doi:10.1029/2001JB001194.
Gurnis, M. (1989), A reassessment of the heat transport by variable viscosity convection with plate and lids, *Geophys. Res. Lett.*, *16*, 179–182.
Hager, B. H., and M. A. Richards (1989), Long-wavelength variations in Earth's geoid: Physical models and dynamic implications, *Philos. Trans. R. Soc. London, Ser. A*, *328*, 309–327.
Huang, J. S., S. J. Zhong, and J. van Hunen (2003), Controls on sublithospheric small-scale convection, *J. Geophys. Res.*, *108*(B8), 2405, doi:10.1029/2003JB002456.
Jarvis, G. T., and W. R. Peltier (1982), Mantle convection as a boundary layer phenomenon, *Geophys. J. R. Astron. Soc.*, *68*, 389–427.
Jellinek, A. M., H. M. Gonnermann, and M. A. Richards (2003), Plume capture by divergent plate motions: Implications for the distribution of hotspots, geochemistry of mid-ocean ridge basalts, and estimates of the flux at the core-mantle boundary, *Earth Planet. Sci. Lett.*, *205*, 361–378.
Karato, S. I., and P. Wu (1993), Rheology of the upper mantle: A synthesis, *Science*, *260*, 771–778.
Katzman, R., L. Zhao, and T. H. Jordan (1998), High-resolution, two-dimensional vertical tomography of the central Pacific mantle using *ScS* reverberations and frequency-dependent travel times, *J. Geophys. Res.*, *103*, 17,933–17,971.
Kennett, B. L. N., and K. Yoshizawa (2002), A reappraisal of regional surface wave tomography, *Geophys. J. Int.*, *150*, 37–44.
King, S. D., and B. H. Hager (1990), The relationship between plate velocity and trench viscosity in Newtonian and power-law subduction calculation, *Geophys. Res. Lett.*, *17*, 2409–2412.
King, S. D., C. W. Gable, and S. A. Weinstein (1992), Models of convection-driven tectonic plates: A comparison of methods and results, *Geophys. J. Int.*, *109*, 481–487.
King, S. D., J. P. Lowman, and C. W. Gable (2002), Episodic tectonic plate reorganizations driven by mantle convection, *Earth Planet. Sci. Lett.*, *203*, 83–91.
Korenaga, J., and T. H. Jordan (2003), Physics of multiscale convection in Earth's mantle: Onset of sublithospheric convection, *J. Geophys. Res.*, *108*(B7), 2333, doi:10.1029/2002JB001760.
Lister, C. R. B., J. G. Sclater, E. E. Davis, H. Villinger, and S. Nagihara (1990), Heat flow maintained in ocean basins of great age: Investigations in the north-equatorial west Pacific, *Geophys. J. Int.*, *102*, 603–630.
Lithgow-Bertelloni, C., and M. A. Richards (1998), The dynamics of Cenozoic and Mesozoic plate motions, *Rev. Geophys.*, *36*, 27–78.
Lithgow-Bertelloni, C., and P. G. Silver (1998), Dynamic topography, plate driving forces and the African superswell, *Nature*, *395*, 269–272.
Lowman, J. P., and C. W. Gable (1999), Thermal evolution of the mantle following continental aggregation in 3D convection models, *Geophys. Res. Lett.*, *26*, 2649–2652.
Lowman, J. P., S. D. King, and C. W. Gable (2003), The role of the heating model of the mantle in intermittent reorganization of the plate velocity field, *Geophys. J. Int.*, *152*, 455–467.
Malamud, B. D., and D. L. Turcotte (1999), How many plumes are there?, *Earth Planet. Sci. Lett.*, *174*, 113–124.
McKenzie, D. P. (1967), Some remarks on heat flow and gravity anomalies, *J. Geophys. Res.*, *72*, 6261–6273.
McKenzie, D. P., J. M. Roberts, and N. O. Weiss (1974), Convection in the mantle: Towards a numerical simulation, *J. Fluid Mech.*, *62*, 465–538.
McNutt, M. K. (1998), Superswell, *Rev. Geophys.*, *36*, 211–244.
Montagner, J. P. (2002), Upper mantle low anisotropy channels below the Pacific plate, *Earth Planet. Sci. Lett.*, *202*, 263–274.
Montelli, R., G. Nolet, F. A. Dahlen, G. Masters, E. R. Engdahl, and S. H. Hung (2004), Finite frequency tomography reveals a variety of plumes in the mantle, *Science*, *303*, 338–343.
Moresi, L. N., and M. Gurnis (1996), Constraints on the lateral strength of slabs from three-dimensional dynamic flow models, *Earth Planet. Sci. Lett.*, *138*, 15–28.
Moresi, L. N., and V. S. Solomatov (1995), Numerical investigation of 2D convection with extremely large viscosity variation, *Phys. Fluids*, *9*, 2154–2164.
Morgan, W. J. (1972), Plate motions and deep mantle convection, *Mem. Geol. Soc. Am.*, *132*, 7–22.
Nyblade, A. A., and S. W. Robinson (1994), The African superswell, *Geophys. Res. Lett.*, *21*, 765–768.
O'Connell, R. J., and B. H. Hager (1980), On the thermal state of the Earth, in *Physics of the Earth's Interior*, edited by A. Dziewonski and E. Boschi, pp. 270–317, Elsevier, New York.
Panasyuk, S. V., and B. Hager (2000), Models of isostatic and dynamic topography, geoid anomalies, and their uncertainties, *J. Geophys. Res.*, *105*, 28,199–28,209.
Parsons, B., and S. F. Daly (1983), The relationship between surface topography, gravity anomalies and temperature structure of convection, *J. Geophys. Res.*, *88*, 1129–1144.
Parsons, B., and D. McKenzie (1978), Mantle convection and thermal structure of the plates, *J. Geophys. Res.*, *83*, 4485–4496.
Parsons, B., and J. G. Sclater (1977), An analysis of the variation of ocean floor bathymetry and heat flow with age, *J. Geophys. Res.*, *82*, 803–827.
Phipps Morgan, J., and W. H. F. Smith (1992), Flattening of the seafloor depth-age curve as a response to asthenospheric flow, *Nature*, *359*, 524–527.
Ribe, N. M., and U. R. Christensen (1994), Three-dimensional modeling of plume-lithosphere interaction, *J. Geophys. Res.*, *99*, 669–683.
Ricard, Y., and C. Vigny (1989), Mantle dynamics with induced plate tectonics, *J. Geophys. Res.*, *94*, 17,543–17,559.
Richter, F. M., and B. Parsons (1975), On the interaction of two scale convection in the mantle, *J. Geophys. Res.*, *80*, 2529–2541.
Ritzwoller, M. H., N. M. Shapiro, and S. Zhong (2004), Cooling history of the Pacific lithosphere, *Earth Planet. Sci. Lett.*, *226*, 69–84.
Romanowicz, B., and Y. C. Gung (2002), Superplumes from the core-mantle boundary to the lithosphere: Implications for heat flux, *Science*, *296*, 513–516.
Schroeder, W. (1984), The empirical age-depth relation and depth anomalies in the Pacific ocean basin, *J. Geophys. Res.*, *89*, 9873–9883.
Sleep, N. H. (1987), Lithospheric heating by mantle plumes, *Geophys. J. R. Astron. Soc.*, *91*, 1–11.
Sleep, N. H. (1990), Hotspots and mantle plumes, some phenomenology, *J. Geophys. Res.*, *95*, 6715–6736.
Solomatov, V. S., and L. N. Moresi (2000), Scaling of time-dependent stagnant convection: Application to small-scale convection on Earth and other terrestrial planets, *J. Geophys. Res.*, *105*, 21,795–21,817.
Stein, C. A., and S. Stein (1992), A model for the global variation in oceanic depth and heat flow with lithospheric age, *Nature*, *359*, 123–129.
Thoraval, C., and M. A. Richards (1997), The geoid constraint in global geodynamics: Viscosity structure, mantle heterogeneity models and boundary conditions, *Geophys. J. Int.*, *131*, 1–8.
Thoraval, C., P. Machetel, and A. Cazenave (1995), Locally layered convection inferred from dynamic models of the Earth's mantle, *Nature*, *375*, 777–780.
Turcotte, D. L., and G. Schubert (2002), *Geodynamics*, 2nd ed. Cambridge Univ. Press, New York.

van Hunen, J., J. Huang, and S. Zhong (2003), The effect of shearing on the onset and vigor of small-scale convection in a Newtonian rheology, *Geophys. Res. Lett.*, *30*(19), 1991, doi:10.1029/2003GL018101.

von Herzen, R. P., M. J. Cordery, R. S. Detrick, and C. Fang (1989), Heat flow and the thermal origin of hot spot swells: The Hawaiian swell revisited, *J. Geophys. Res.*, *94*, 13,783–13,799.

Wilson, J. T. (1963), A possible origin of the Hawaiian Islands, *Can. J. Phys.*, *41*, 863–870.

Wolfe, C. J., I. T. Bjarnason, J. C. Vandecar, and S. C. Soloman (1997), Seismic structure of the Iceland mantle plume, *Nature*, *385*, 245–247.

Yuen, D. A., and L. Fleitout (1985), Thinning of the lithosphere by small-scale convective destabilization, *Nature*, *313*, 125–128.

Zaranek, S. E., and E. M. Parmentier (2004), The onset of convection in fluids with strongly temperature-dependent viscosity cooled from above with implications for planetary lithospheres, *Earth Planet. Sci. Lett.*, *224*, 371–386.

Zhong, S., and M. Gurnis (1994), Role of plate and temperature-dependent viscosity in phase change dynamics, *J. Geophys. Res.*, *99*, 15,903–15,917.

Zhong, S., and M. Gurnis (1995), Mantle convection with plates and mobile, faulted plate margins, *Science*, *267*, 838–843.

Zhong, S., M. T. Zuber, L. N. Moresi, and M. Gurnis (2000), Role of temperature dependent viscosity and surface plates in spherical shell models of mantle convection, *J. Geophys. Res.*, *105*, 11,063–11,082.

J. Huang, Department of Geophysics, School of Geodesy and Geomatics, Wuhan University, Wuhan 430079, China.

S. Zhong (corresponding author), Department of Physics, University of Colorado, Campus Box 390, Boulder, CO 80309, USA. (szhong@anquetil.colorado.edu)